This article has been accepted for publication in IEEE Transactions on Automation Science and Engineering. This is the author's version which has not been fully edited and content may change prior to final publication. Citation information: DOI 10.1109/TASE.2026.3654151

MCTP: A Multi-Coupled Dynamics Trajectory Planning Scheme for Autonomous Driving in Extreme Conditions

Xuepeng Hu, Yu Zhang, Chengye Wang, Shi, Shaoyang, Zhenfeng Wang, Yechen Qin, *IEEE Senior Member*

***Abstract*—Trajectory planning is essential for ensuring the safe operation of autonomous vehicles. However, existing methods rarely consider the vehicle's multi-coupled dynamics, including lateral-longitudinal motion coupling, tire force coupling, and lateral instability. This omission can result in infeasible trajectories, vehicle instability, or even accidents under extreme conditions. To address this challenge, this study presents a multi-coupled dynamics trajectory planning (MCTP) scheme. MCTP establishes a coupled kinematics model to accurately represent vehicle motion states and constructs a tire force representation model, which based solely on vehicle motion states, facilitating seamless integration into trajectory planning. By incorporating coupled tire force characteristics and lateral stability analysis, a set of coupled dynamic constraints is formulated to ensure trajectory feasibility and lateral stability. Additionally, a multi-objective function is designed to further optimize trajectory safety, dynamic feasibility, and lateral stability, with the optimal trajectory obtained through receding horizon optimization. Closed-loop validation on both hardware-in-the-loop and real-vehicle experimental platforms demonstrates that, MCTP generates trajectories with enhanced safety and feasibility. It also improves tracking stability margins and dynamics performance, highlighting its effectiveness in handling extreme conditions.**

***Note to Practitioners*—This paper was motivated by the problem of optimal trajectory planning for autonomous vehicles under extreme conditions. In such conditions, the multi-coupled dynamics of the vehicle become prominent, making it highly challenging to generate a trajectory that is safe, dynamically feasible, and laterally stable. To overcome these challenges, this paper proposes a trajectory planning scheme that explicitly considers multi-coupled dynamics. By leveraging vehicle kinematics, dynamics, and stability modeling, the multi-coupled dynamics are transformed into constraints directly related to the vehicle motion states, thereby avoiding the introduction of high-dimensional and complex vehicle and tire dynamics models. Performance metrics are designed to account for safety, feasibility, and stability, forming a multi-objective function that is optimized using nonlinear model predictive control to achieve the optimal trajectory by optimizing multi-dimensional vehicle motion states. Experimental results demonstrate that the proposed scheme significantly enhances trajectory performance, as well as the safety and stability of closed-loop vehicle operation under extreme conditions. In future work, this study will explore the integration of multi-coupled vehicle dynamics into the decision-making layer of autonomous driving.**

***Index Terms*—Trajectory planning, multi-coupled dynamics, multi-objective optimization, closed-loop validation.**

I. Introduction

AUTONOMOUS vehicles (AVs) have attracted widespread attention due to their potential in enhancing traffic safety, energy utilization, and transportation efficiency [1]. As a critical module in autonomous driving systems (ADS), trajectory planning integrates perception data to generate open-loop trajectories for low-level controllers, directly influencing system safety and intelligence [2], [3].

Numerous methods have been proposed to continuously improve the performance of trajectory planners. However, trajectory planning under extreme conditions, such as high-speed overtaking and emergency collision avoidance on slippery roads, poses significant challenges to conventional trajectory planning. These maneuvers introduce multi-coupled dynamics, requiring precise motion planning and control to achieve both safety and stability. Therefore, further research on trajectory planning under extreme conditions is essential [4].

A. Related Works

To tackle trajectory planning problems, researchers have explored various methods, which can be broadly classified into five categories: sampling-based, graph search-based, curve interpolation-based, numerical optimization-based, and learning-based methods [5]–[8]. These methods typically focus on spatiotemporal collision avoidance constraints and vehicle interaction modeling to enhance safety and efficiency in complex traffic scenarios [9]–[11]. However, most existing methods simplify or overlook the multi-coupled dynamics characteristics of vehicles, which can result in trajectories that are difficult to track or even dynamically infeasible during extreme conditions, thereby compromising vehicle safety and lateral stability [12]. To improve the performance of AVs under such maneuvers, trajectory planning methods have been refined with maneuver-specific considerations [13], [14]. These methods incorporate simplified vehicle dynamic characteristics, such as maximum lateral acceleration constraints, enhancing the feasibility of the trajectory. Nevertheless, they do not account for deeper tire dynamics, still risk generating

This paper never present at a conference or submit elsewhere previously.

This work was supported in part by the National Natural Science Foundation of China under Grant 52522218, 52272386 and 52502495, in part by the Fundamental Research Funds for the Central Universities. *(Corresponding author: Yechen Qin; Zhenfeng Wang.)*

Xuepeng Hu, Yu Zhang, Chengye Wang, Shi, Shaoyang and Yechen Qin are with School of Mechanical Engineering, Beijing Institute of Technology, Beijing, 10081, China. Yu Zhang is also with the China North Vehicle Research Institute, Beijing 100072, China. (E-mails: xpxpxp@bit.edu.cn, zhyss_bit@bit.edu.cn, 3120240328@bit.edu.cn, shishaoyang@bit.edu.cn, and qinyechen@bit.edu.cn).

Zhenfeng Wang is with BYD Automotive Industry Co., Ltd., Shenzhen, 518118, China (e-mail: wangzhenfeng612@gmail.com).

Authorized licensed use limited to: BEIJING INSTITUTE OF TECHNOLOGY. Downloaded on January 18,2026 at 10:57:50 UTC from IEEE Xplore. Restrictions apply.
© 2026 IEEE. All rights reserved, including rights for text and data mining and training of artificial intelligence and similar technologies. Personal use is permitted, but republication/redistribution requires IEEE permission. See https://www.ieee.org/publications/rights/index.html for more information.

This article has been accepted for publication in IEEE Transactions on Automation Science and Engineering. This is the author's version which has not been fully edited and content may change prior to final publication. Citation information: DOI 10.1109/TASE.2026.3654151

infeasible trajectories. This is because the dynamic feasibility of a trajectory is constrained by the ability of the tires to generate sufficient lateral and longitudinal forces to support vehicle motion along the planned trajectory. Some studies have recognized this issue and conducted detailed modeling of both vehicle and tire dynamics [15]–[18], but the complexity and high dimensionality of the system model restrict the prediction horizon, and the extensive parameter calibration required for complex tire models further limits their practical applicability. Recent studies have demonstrated that improving trajectory planning itself enables the use of simpler controllers while achieving higher tracking accuracy and stability [19]. This also underscores the necessity of developing trajectory planning methodologies that explicitly consider multi-coupled dynamics while maintaining reasonable problem simplification [20].

Beyond theoretical formulation, the structure of trajectory planning problems significantly affects performance, leading to two primary paradigms: decoupled and joint planning. Decoupled planning decomposes the three-dimensional trajectory planning problem into two separate two-dimensional subproblems, commonly using path-velocity decoupling (PVD) or lateral-longitudinal decoupling (LLD). This structure is widely applied for its advantages in simplifying problems and improving solution efficiency. In extreme conditions trajectory planning, PVD has been applied to highway lane-change collision avoidance scheme [21]. Similarly, LLD-based studies have investigated trajectory planning considering chassis dynamics [22] and emergency collision avoidance systems with stability guarantees [23]. Despite these successes, decoupled planning shares common limitations: it tends to focus on the geometric aspects of the trajectory, neglecting the vehicle dynamics [24]. For instance, by presetting high-order polynomials for trajectories, these methods restrict flexibility and fail to accurately represent vehicle motion states. Additionally, the vehicle's longitudinal and lateral motions are strongly coupled, and decoupled planning inevitably compromises solution optimality [25]. A more intuitive consequence is that the vehicle may struggle to track trajectories where longitudinal and lateral motions are poorly coordinated, compromising both safety and lateral stability. In contrast, joint planning directly solves the three-dimensional trajectory planning problem. Its potential to generate high-quality solutions while seamlessly integrating with vehicle kinematics model has drawn significant research attention [10]. Although joint planning offers these advantages, its current limitations lie in the urgent need for a simple yet effective method to incorporate the vehicle's multi-coupled dynamics characteristics, especially for handling extreme driving conditions [20], [26]. To address these limitations, some studies have developed vehicle motion envelopes [27], enabling high-performance trajectory planning. However, this approach does not consider the optimization of the vehicle lateral motion states and requires specific envelope parameterization.

In summary, a fundamental challenge remains in how to effectively incorporate the vehicle's dynamic characteristics into trajectory planning, accurately represent, constrain, and optimize the multiple vehicle motion states, while ensuring the optimality of the trajectory.

B. Motivations and Contributions

Motivated by the aforementioned issues, this study proposes a multi-coupled dynamics trajectory planning (MCTP) scheme. First, a tire force representation model (TFRM) is introduced to incorporate multi-coupled vehicle dynamics into trajectory planning. By integrating tire force coupling characteristics with lateral stability analysis, MCTP formulates coupled dynamic constraints. Then, to accurately represent, constrain, and optimize multiple vehicle motion states, MCTP integrates a coupled kinematics model, coupled dynamic constraints, and a multi-objective function incorporating multiple performance metrics. The optimal trajectory is then obtained using nonlinear model predictive control (NMPC). Finally, closed-loop validation is conducted on both hardware-in-the-loop (HiL) and real-vehicle experimental platforms to evaluate the performance of MCTP. The main contributions of this paper are summarized below:

- A vehicle motion states-based TFRM is developed to represent longitudinal and lateral tire forces for each wheel without relying on complex tire modeling and specific tire model parameters, enables the incorporation of multi-coupled vehicle dynamics into trajectory planning in the form of state constraints.
- The MCTP scheme is proposed, integrating coupled kinematics model, coupled dynamic constraints, and multi-objective function constructed with multiple performance metrics, employing NMPC to obtain the optimal trajectory. Aiming to enhance the safety, feasibility, and lateral stability of trajectories during extreme conditions.
- The HiL and real-vehicle experimental platforms were established to validate the closed-loop effectiveness and real-time performance of MCTP.

C. Organization

The rest of this paper is structured as follows. An overview of MCTP is provided in Section II. The system and TFRM modeling are introduced in Section III. The details of MCTP methodology are illustrated in Section IV. Section V discusses the experiments results of the MCTP based on HiL and real-vehicle experimental platform. Finally, the paper is summarized, and conclusions are drawn in Section VI.

II. System Overview

The framework of the proposed MCTP is illustrated in Fig. 1. MCTP formulates an NMPC problem, which consists of a prediction model, multi-constraints, and a multi-objective function. The prediction model is constructed based on a coupled kinematics model to accurately predict and represent the vehicle's motion states. A vehicle dynamics model is established, and by considering load transfer and the driving characteristics of distributed drive electric vehicles (DDEVs), the TFRM is derived to map vehicle-level motion states to component-level tire forces. Based on the tire forces represented by TFRM and their coupling characteristics, dynamic feasibility constraints are formulated, while lateral stability constraints are obtained through stability analysis. These two

Authorized licensed use limited to: BEIJING INSTITUTE OF TECHNOLOGY. Downloaded on January 18,2026 at 10:57:50 UTC from IEEE Xplore. Restrictions apply.
© 2026 IEEE. All rights reserved, including rights for text and data mining and training of artificial intelligence and similar technologies. Personal use is permitted, but republication/redistribution requires IEEE permission. See https://www.ieee.org/publications/rights/index.html for more information.

This article has been accepted for publication in IEEE Transactions on Automation Science and Engineering. This is the author's version which has not been fully edited and content may change prior to final publication. Citation information: DOI 10.1109/TASE.2026.3654151

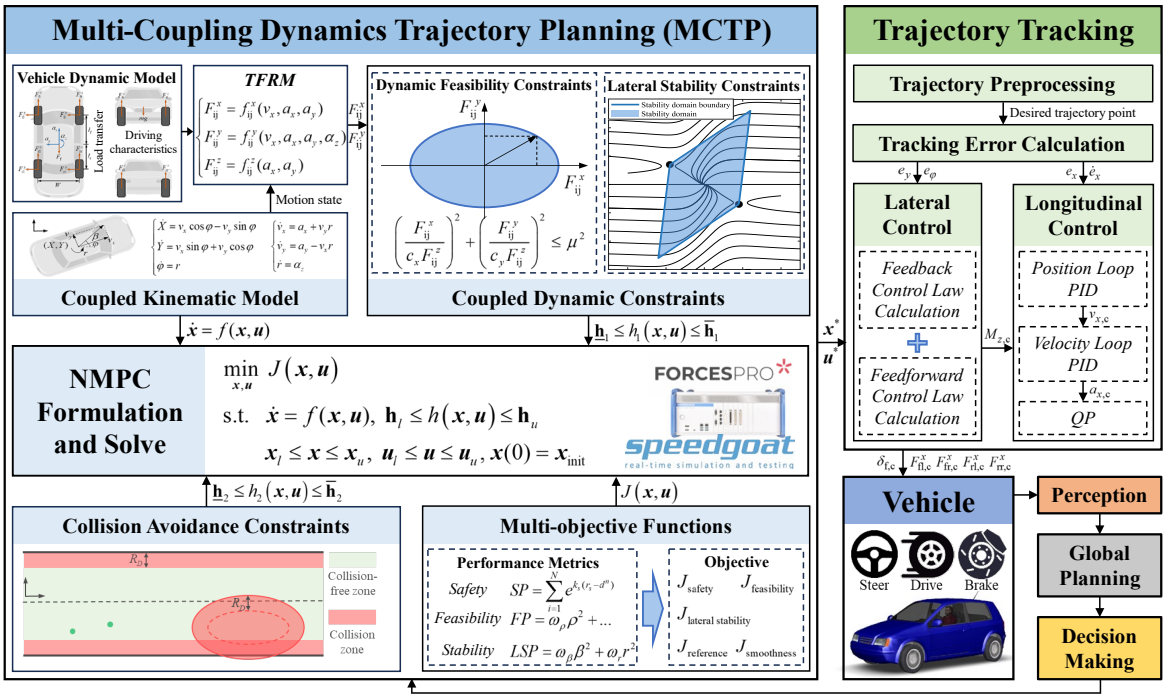


Fig. 1. Multi-coupled dynamics trajectory planning framework.

types of constraints jointly form the coupled dynamics constraints, ensuring that the vehicle's multi-coupled dynamics are considered at the trajectory planning level through comprehensive motion states constraints. The collision avoidance constraint is constructed using geometric representation of the vehicle contour and dual modeling. A set of multi-dimensional performance metrics targeting trajectory safety, feasibility, and stability is designed. Based on these metrics, a multi-objective function for trajectory planning is formulated to optimize the vehicle's multiple motion states. Finally, the NMPC problem is constructed and solved using a receding horizon optimization approach to compute the optimal trajectory.

III. Vehicle and TFRM Modeling

This section primarily introduces the vehicle models employed in MCTP and the details of TFRM.

A. Coupled Kinematics Model

The vehicle kinematics model is crucial to constrain the trajectory and improve the feasibility. As illustrated in Fig. 2(a), this work incorporates the full vehicle kinematics to more accurately capture the coupling between longitudinal and lateral motions. The corresponding equations of motion are:

$$\begin{cases} \dot{X} = v_x \cos\varphi - v_y \sin\varphi \\ \dot{Y} = v_x \sin\varphi + v_y \cos\varphi \\ \dot{\varphi} = r \\ \dot{v}_x = a_x + v_y r \\ \dot{v}_y = a_y - v_x r \\ \dot{r} = \alpha_z \end{cases} \tag{1}$$

where X and Y denote the longitudinal and lateral position of the center of gravity (CG) in the global coordinate system (GCS), and φ represents the vehicle's yaw angle. The variables v_x, v_y, r, a_x, a_y and α_z correspond to the longitudinal velocity, lateral velocity, yaw rate, longitudinal acceleration, lateral acceleration, and yaw angular acceleration of the CG in the vehicle coordinate system, respectively.

B. Vehicle Dynamics Model

For trajectory planning, vehicle dynamics are modeled at the vehicle level. As shown in Fig. 2(b), the overall vehicle dynamics can be described by the following equations [28]:

$$\begin{cases} ma_x = F_{\mathrm{fl}}^x + F_{\mathrm{fr}}^x + F_{\mathrm{rl}}^x + F_{\mathrm{rr}}^x - F_{\mathrm{f}} \\ ma_y = F_{\mathrm{fl}}^y + F_{\mathrm{fr}}^y + F_{\mathrm{rl}}^y + F_{\mathrm{rr}}^y \\ I_z\alpha_z = \frac{W}{2}(-F_{\mathrm{fl}}^x + F_{\mathrm{fr}}^x - F_{\mathrm{rl}}^x + F_{\mathrm{rr}}^x) + \\ \qquad l_{\mathrm{f}}(F_{\mathrm{fl}}^y + F_{\mathrm{fr}}^y) - l_{\mathrm{r}}(F_{\mathrm{rl}}^y + F_{\mathrm{rr}}^y) \end{cases} \tag{2}$$

where m corresponds to the mass of the vehicle, I_z is the yaw inertia, W denotes the wheel track, l_{f} and l_{r} are the distances from the CG to the front and rear axle, respectively. F_{ij}^x and F_{ij}^y are longitudinal and lateral tire forces, ij $= \{$fl,fr,rl,rr$\}$ indicate the front left, front right, rear left, and rear right wheels, respectively. F_{f} is the driving resistance, $F_{\mathrm{f}} = mgf + \frac{1}{2}C_D A\rho(v_x + v_{\mathrm{air}})^2 + mg\sin\theta$. Parameters g, f, C_D, A, ρ, v_{air} and θ represent the gravitational acceleration, rolling resistance coefficient, aerodynamic drag coefficient, frontal area, air density, air flow velocity and road gradient.

C. TFRM Modeling

DDEVs are ideal platforms for ADS, as they can maximize vehicle mobility, especially in extreme conditions [14]. Therefore, this study uses DDEVs as the foundational research subject. The proposed TFRM is developed by integrating the

Authorized licensed use limited to: BEIJING INSTITUTE OF TECHNOLOGY. Downloaded on January 18,2026 at 10:57:50 UTC from IEEE Xplore. Restrictions apply.
© 2026 IEEE. All rights reserved, including rights for text and data mining and training of artificial intelligence and similar technologies. Personal use is permitted, but republication/redistribution requires IEEE permission. See https://www.ieee.org/publications/rights/index.html for more information.

This article has been accepted for publication in IEEE Transactions on Automation Science and Engineering. This is the author's version which has not been fully edited and content may change prior to final publication. Citation information: DOI 10.1109/TASE.2026.3654151

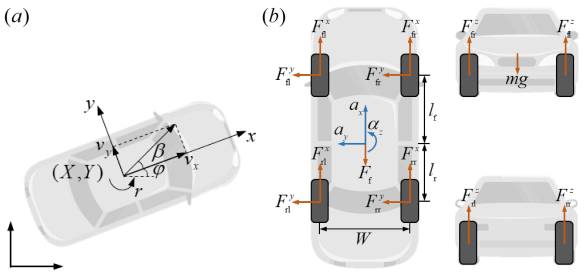


Fig. 2. Vehicle model. (a) Vehicle kinematics model with coupled longitudinal and lateral motion. (b) Vehicle dynamics model.

vehicle dynamics model while considering load transfer and DDEVs's driving characteristics.

For the entire vehicle, the vertical forces at each tire considering load transfer are obtained as follows:

$$\begin{cases} F_{\mathrm{fl}}^z = \frac{mgl_{\mathrm{r}}}{2L} - \frac{ma_x h}{2L} - \frac{ma_y h l_{\mathrm{r}}}{WL} \\ F_{\mathrm{fr}}^z = \frac{mgl_{\mathrm{r}}}{2L} - \frac{ma_x h}{2L} + \frac{ma_y h l_{\mathrm{r}}}{WL} \\ F_{\mathrm{rl}}^z = \frac{mgl_{\mathrm{f}}}{2L} + \frac{ma_x h}{2L} - \frac{ma_y h l_{\mathrm{f}}}{WL} \\ F_{\mathrm{rr}}^z = \frac{mgl_{\mathrm{f}}}{2L} + \frac{ma_x h}{2L} + \frac{ma_y h l_{\mathrm{f}}}{WL} \end{cases} \tag{3}$$

where h denotes the height of the CG, L is the wheelbase, and F_{ij}^z represent the tire vertical forces.

For DDEVs, the longitudinal force at each tire is typically allocated in proportion to its vertical load [29], therefore:

$$\frac{F_{\mathrm{fl}}^x}{F_{\mathrm{fl}}^z} = \frac{F_{\mathrm{fr}}^x}{F_{\mathrm{fr}}^z} = \frac{F_{\mathrm{rl}}^x}{F_{\mathrm{rl}}^z} = \frac{F_{\mathrm{rr}}^x}{F_{\mathrm{rr}}^z} = \frac{\sum F_{\mathrm{ij}}^x}{\sum F_{\mathrm{ij}}^z} \tag{4}$$

Based on (2)-(4), the tire longitudinal force is given by $F_{\mathrm{ij}}^x = \frac{ma_x + F_{\mathrm{f}}}{mg} F_{\mathrm{ij}}^z$, by incorporating the lateral and yaw dynamic equations presented in (2), the following is derived:

$$\begin{cases} F_{\mathrm{fl}}^y + F_{\mathrm{fr}}^y = \frac{ma_y l_{\mathrm{r}} + I_z \alpha_z}{L} - \frac{(ma_x + F_{\mathrm{f}}) a_y h}{gL} \\ F_{\mathrm{rl}}^y + F_{\mathrm{rr}}^y = \frac{ma_y l_{\mathrm{f}} - I_z \alpha_z}{L} + \frac{(ma_x + F_{\mathrm{f}}) a_y h}{gL} \end{cases} \tag{5}$$

Once the lateral forces of the front and rear axles are determined, the lateral forces of each tire can be calculated proportionally based on the vertical loads of the respective tires [30], and therefore:

$$\begin{cases} F_{\mathrm{fl}}^y = \frac{F_{\mathrm{fl}}^y + F_{\mathrm{fr}}^y}{F_{\mathrm{fl}}^z + F_{\mathrm{fr}}^z} F_{\mathrm{fl}}^z, F_{\mathrm{fr}}^y = \frac{F_{\mathrm{fl}}^y + F_{\mathrm{fr}}^y}{F_{\mathrm{fl}}^z + F_{\mathrm{fr}}^z} F_{\mathrm{fr}}^z \\ F_{\mathrm{rl}}^y = \frac{F_{\mathrm{rl}}^y + F_{\mathrm{rr}}^y}{F_{\mathrm{rl}}^z + F_{\mathrm{rr}}^z} F_{\mathrm{rl}}^z, F_{\mathrm{rr}}^y = \frac{F_{\mathrm{rl}}^y + F_{\mathrm{rr}}^y}{F_{\mathrm{rl}}^z + F_{\mathrm{rr}}^z} F_{\mathrm{rr}}^z \end{cases} \tag{6}$$

The proposed TFRM is derived by combining (2)-(6), the detailed expression is provided in the Appendix. For simplicity, the corresponding mapping relationship between the vehicle's longitudinal, lateral, and vertical tire forces and its motion states can be reformulated as:

$$\begin{cases} F_{\mathrm{ij}}^x = f_{\mathrm{ij}}^x(v_x, a_x, a_y) \\ F_{\mathrm{ij}}^y = f_{\mathrm{ij}}^y(v_x, a_x, a_y, \alpha_z) \\ F_{\mathrm{ij}}^z = f_{\mathrm{ij}}^z(a_x, a_y) \end{cases} \tag{7}$$

where $f_{\mathrm{ij}}^x(\cdot)$, $f_{\mathrm{ij}}^y(\cdot)$ and $f_{\mathrm{ij}}^z(\cdot)$ represent the characteristic functions of the longitudinal, lateral, and vertical tire forces of TFRM at different wheels, respectively.

As shown in Eq. 7, TFRM establishes a mapping between vehicle-level motion states (e.g., v_x, a_x, a_y) and tire forces without relying on complex tire dynamics or empirical parameters. This enables the direct incorporation of multi-coupled dynamics (e.g., lateral-longitudinal force coupling, load transfer and lateral instability) into trajectory planning as state-dependent constraints.

IV. Multi-coupled Dynamics Trajectory Planning Methodology

This section presents the design and key components of NMPC-based MCTP in detail.

A. Nonlinear Prediction Model

The prediction model is fundamental for feasible trajectory planning, as it accurately predicts the vehicle's motion states and helps define state and input constraints in the optimal control problem (OCP). Based on the coupled kinematics model, vehicle acceleration is chosen as the input, and the slack factors (s_1 and s_2) are augmented in the input to facilitate the solution of the OCP; the remaining vehicle motion states serve as the states. The nonlinear prediction model is expressed as follows:

$$\dot{\boldsymbol{x}} = f(\boldsymbol{x}, \boldsymbol{u}) \tag{8}$$

where $\boldsymbol{x} = [X, Y, \varphi, v_x, v_y, r]^{\mathrm{T}}$ represents the state, $\boldsymbol{u} = [a_x, a_y, \alpha_z, s_1, s_2]^{\mathrm{T}}$ represents the input, and $f(\cdot)$ is the nonlinear function.

B. Coupled Dynamics Constraints

This study incorporates multi-coupled dynamics characteristics as constraints in trajectory planning, including dynamic feasibility and lateral stability constraints.

1) Dynamic Feasibility Constraints: The vehicle's motion is driven by tire forces, during extreme conditions, the coupling between longitudinal and lateral tire forces becomes significant, and the maximum tire force is limited by road adhesion. Therefore, dynamic feasibility constraints are enforced by limiting the tire forces accordingly.

Combined with the previously derived TFRM (7), the tire friction ellipse shown in Fig. 1 can be converted into the dynamic feasibility constraints, written as:

$$\left(\frac{f_{\mathrm{ij}}^x(v_x, a_x, a_y)}{c_x f_{\mathrm{ij}}^z(a_x, a_y)} \right)^2 + \left(\frac{f_{\mathrm{ij}}^y(v_x, a_x, a_y, \alpha_z)}{c_y f_{\mathrm{ij}}^z(a_x, a_y)} \right)^2 \leq \mu^2 \tag{9}$$

where the constant c_x and c_y are proportionality factor related to the tire characteristics, and μ is the road adhesion coefficient. When the coupled vehicle motion states satisfy (9), the planned trajectory is dynamically feasible.

2) Lateral Stability Constraints: During extreme conditions, the vehicle is prone to lateral instability. Excessive yaw rates can cause side-slip, fishtailing, or even rollover, while rear axle lateral force saturation may lead to oversteering. Therefore, appropriate constraints are needed to maintain lateral motion states within a controllable range.

The $\beta - r$ phase plane is suitable for stability analysis. In this plane, the vehicle's stability domain is represented by a parallelogram-shaped region [31], as shown in Fig. 1. To better utilize the vehicle's handling limits [32] while simplifying the

Authorized licensed use limited to: BEIJING INSTITUTE OF TECHNOLOGY. Downloaded on January 18,2026 at 10:57:50 UTC from IEEE Xplore. Restrictions apply.
© 2026 IEEE. All rights reserved, including rights for text and data mining and training of artificial intelligence and similar technologies. Personal use is permitted, but republication/redistribution requires IEEE permission. See https://www.ieee.org/publications/rights/index.html for more information.

This article has been accepted for publication in IEEE Transactions on Automation Science and Engineering. This is the author's version which has not been fully edited and content may change prior to final publication. Citation information: DOI 10.1109/TASE.2026.3654151

OCP, slack factors are introduced to adjust the lateral motion states. The lateral stability constraints are then reformulated as:

$$\boldsymbol{\Gamma x} \leq \mathbf{K} + \mathbf{S}\boldsymbol{u} \tag{10}$$

the matrices and vectors are:

$$\boldsymbol{\Gamma} = \begin{bmatrix} 0 & 0 & 0 & 0 & 0 & v_x \\ 0 & 0 & 0 & 0 & 0 & -v_x \\ 0 & 0 & 0 & 0 & \frac{1}{v_x} & -\frac{l_\mathrm{r}}{v_x} \\ 0 & 0 & 0 & 0 & -\frac{1}{v_x} & \frac{l_\mathrm{r}}{v_x} \end{bmatrix}, \quad \mathbf{K} = \begin{bmatrix} \mu g & \mu g & \alpha_{\mathrm{r,sat}} & \alpha_{\mathrm{r,sat}} \end{bmatrix}^\mathrm{T}, \quad \mathbf{S} = \begin{bmatrix} 0 & 0 & 0 & \mu g & 0 \\ 0 & 0 & 0 & \mu g & 0 \\ 0 & 0 & 0 & 0 & \alpha_{\mathrm{r,sat}} \\ 0 & 0 & 0 & 0 & \alpha_{\mathrm{r,sat}} \end{bmatrix}.$$

where $\beta = \frac{v_y}{v_x}$, $\alpha_{\mathrm{r,sat}}$ is the saturation slip angle of the rear tire, and the constraints for the slack factors are given as: $0 \leq s_1 \leq 0.05$, $0 \leq s_2 \leq 0.1$.

C. Collision Avoidance Constraints

Collision avoidance constraints ensure the ego vehicle avoids obstacles within the planning horizon.

The modeling of collision avoidance constraints is shown in Fig. 3, two circles with same radius ($R_D = \sqrt{\frac{1}{4}W^2 + \frac{1}{16}(L + L_\mathrm{f} + L_\mathrm{r})^2}$) are used to cover the ego vehicle. The positions of the circle centers in the GCS are:

$$\begin{cases} X_\mathrm{f} = X + (\frac{1}{4}(3L + 3L_\mathrm{f} - L_\mathrm{r}) - l_\mathrm{r})\cos\varphi \\ Y_\mathrm{f} = Y + (\frac{1}{4}(3L + 3L_\mathrm{f} - L_\mathrm{r}) - l_\mathrm{r})\sin\varphi \\ X_\mathrm{r} = X + (\frac{1}{4}(L + L_\mathrm{f} - 3L_\mathrm{r}) - l_\mathrm{r})\cos\varphi \\ Y_\mathrm{r} = Y + (\frac{1}{4}(L + L_\mathrm{f} - 3L_\mathrm{r}) - l_\mathrm{r})\sin\varphi \end{cases} \tag{11}$$

where X_m and Y_m are the longitudinal and lateral position of the CG in the GCS, $\mathrm{m} = \{\mathrm{f}, \mathrm{r}\}$ represent the circle near the front axle and the rear axle. L_f and L_r represent the front and rear overhang of the ego vehicle, respectively.

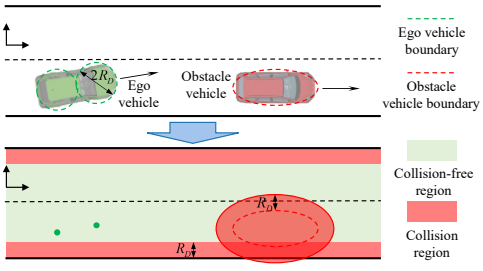


Fig. 3. Collision avoidance constraints modeling.

The obstacle vehicle is covered by an ellipse, and the collision avoidance constraints ensure that the centers of the two circles remain outside the expanded elliptical obstacle region (enlarged by R_D) [33]. By combining the positions of the circle centers and the boundary equation of the expanded elliptical obstacle region, the collision avoidance constraints can be formulated as:

$$\begin{cases} {\boldsymbol{x}^n_{\mathrm{ell,f}}}^\mathrm{T} \boldsymbol{P}^n \boldsymbol{x}^n_{\mathrm{ell,f}} \geq 1 \\ {\boldsymbol{x}^n_{\mathrm{ell,r}}}^\mathrm{T} \boldsymbol{P}^n \boldsymbol{x}^n_{\mathrm{ell,r}} \geq 1 \end{cases} \tag{12}$$

where $\boldsymbol{x}^n_{\mathrm{ell,f}} = \begin{bmatrix} X_\mathrm{f} - X^n_{\mathrm{obs}} \\ Y_\mathrm{f} - Y^n_{\mathrm{obs}} \end{bmatrix}$, $\boldsymbol{x}^n_{\mathrm{ell,r}} = \begin{bmatrix} X_\mathrm{r} - X^n_{\mathrm{obs}} \\ Y_\mathrm{r} - Y^n_{\mathrm{obs}} \end{bmatrix}$, $\boldsymbol{P}^n = \begin{bmatrix} \frac{\cos^2\varphi^n_{\mathrm{obs}}}{{a^n_{\mathrm{obs}}}^2} + \frac{\sin^2\varphi^n_{\mathrm{obs}}}{{b^n_{\mathrm{obs}}}^2} & \cos\varphi^n_{\mathrm{obs}}\sin\varphi^n_{\mathrm{obs}}(\frac{1}{{a^n_{\mathrm{obs}}}^2} - \frac{1}{{b^n_{\mathrm{obs}}}^2}) \\ \cos\varphi^n_{\mathrm{obs}}\sin\varphi^n_{\mathrm{obs}}(\frac{1}{{a^n_{\mathrm{obs}}}^2} - \frac{1}{{b^n_{\mathrm{obs}}}^2}) & \frac{\sin^2\varphi^n_{\mathrm{obs}}}{{a^n_{\mathrm{obs}}}^2} + \frac{\cos^2\varphi^n_{\mathrm{obs}}}{{b^n_{\mathrm{obs}}}^2} \end{bmatrix}$, $a^n_{\mathrm{obs}} = \frac{1}{2}L^n_{\mathrm{obs}} + R_D$, $b^n_{\mathrm{obs}} = \frac{1}{2}W^n_{\mathrm{obs}} + R_D$. The variables X^n_{obs}, Y^n_{obs}, φ^n_{obs}, L^n_{obs} and W^n_{obs} correspond to the longitudinal position, lateral position, yaw angle, length and width of the n-th obstacle vehicle's center in the GCS, respectively.

D. Performance Metrics and Objective Function

This subsection defines three key metrics — safety, feasibility, and lateral stability. These metrics serve as optimization objectives in the OCP's objective function, guiding the generation of high-quality trajectories.

1) Safety Performance Metric: Safety is measured by the distance between trajectory and obstacles. If this distance falls below a safety threshold, the collision risk rises sharply. An exponential function defines the safety performance metric:

$$SP = \sum_{i=1}^{N} e^{k_s(r_s - d^n)} \tag{13}$$

where $d^n = (X - X^n_{\mathrm{obs}})^2 + (Y - Y^n_{\mathrm{obs}})^2$, k_s is a proportional factor, and r_s is the safety distance threshold.

2) Feasibility Performance Metric: Curvature significantly affects trajectory feasibility. High curvature may make trajectories untrackable or even cause side-slip at high speeds. Planned acceleration also impacts feasibility. Since acceleration relies on tire-road friction, excessive acceleration can hinder accurate tracking, especially on low-adhesion road. Thus, the feasibility performance metric can be defined as:

$$FP = \omega_\rho \rho^2 + \omega_{a_x} {a_x}^2 + \omega_{a_y} {a_y}^2 + \omega_{\alpha_z} {\alpha_z}^2 \tag{14}$$

where curvature $\rho = \frac{r}{v_x}$. The weights ω_ρ, ω_{a_x}, ω_{a_y} and ω_{α_z} represent the importance of each term.

3) Lateral Stability Performance Metric: In vehicle lateral stability analysis, slip angle and yaw rate directly indicate tire lateral force saturation and side-slip risk. Excessive values of either can cause instability. Thus, the lateral stability performance metric is defined as:

$$LSP = \omega_\beta \beta^2 + \omega_r r^2 \tag{15}$$

where ω_β and ω_r are the weights corresponding to the slip angle and yaw rate, respectively.

4) Objective Function: To enhance the safety, feasibility, and lateral stability of the trajectory, the optimization objectives over the entire prediction horizon are designed based on the multi-dimensional performance metrics, which include:

$$\begin{cases} J_{\mathrm{safety}} = \omega_{SP} \int_t^{t+T_\mathrm{p}} SP dt \\ J_{\mathrm{feasibility}} = \int_t^{t+T_\mathrm{p}} FP dt \\ J_{\mathrm{lateral\,stability}} = \int_t^{t+T_\mathrm{p}} LSP dt \end{cases} \tag{16}$$

where ω_{SP} is the safety performance weight, $T_\mathrm{p} = N_\mathrm{p}\Delta t$ is the prediction horizon, N_p is the number of prediction steps, and Δt is the discrete time step.

Authorized licensed use limited to: BEIJING INSTITUTE OF TECHNOLOGY. Downloaded on January 18,2026 at 10:57:50 UTC from IEEE Xplore. Restrictions apply.
© 2026 IEEE. All rights reserved, including rights for text and data mining and training of artificial intelligence and similar technologies. Personal use is permitted, but republication/redistribution requires IEEE permission. See https://www.ieee.org/publications/rights/index.html for more information.

This article has been accepted for publication in IEEE Transactions on Automation Science and Engineering. This is the author's version which has not been fully edited and content may change prior to final publication. Citation information: DOI 10.1109/TASE.2026.3654151

In addition, to ensure driving efficiency and avoid unnecessary deviations from the reference state $\boldsymbol{x}_{\text{ref}}$, the reference objective function is formulated as:

$$J_{\text{reference}} = \omega_{\text{ref}} \int_{t}^{t+T_{\text{p}}} (\boldsymbol{x} - \boldsymbol{x}_{\text{ref}})^2 dt \tag{17}$$

where ω_{ref} is the reference objective weight.

To ensure smooth OCP output, the input derivative defines the smoothness objective function as follows:

$$J_{\text{smoothness}} = \int_{t}^{t+T_{\text{p}}} \left[\begin{array}{l} \omega_{j_x} (\frac{da_x}{dt})^2 + \omega_{j_y} (\frac{da_y}{dt})^2 \\ +\omega_{j_z} (\frac{d\alpha_z}{dt})^2 \end{array} \right] dt \tag{18}$$

where ω_{j_x}, ω_{j_y} and ω_{j_z} are the smoothness weights for the respective input.

Combining the above objectives, the multi-objective function is as follows:

$$\begin{aligned} J(\boldsymbol{x}, \boldsymbol{u}) = J_{\text{safety}} + J_{\text{feasibility}} + J_{\text{lateral stability}} \\ + J_{\text{reference}} + J_{\text{smoothness}} \end{aligned} \tag{19}$$

This work focuses on extreme conditions. Therefore, the weight settings prioritize safety, feasibility, and lateral stability. Under normal conditions, increasing the reference and smoothness weights enhances driving efficiency and comfort.

E. NMPC Problem Formulation

Based on the prediction model, multi-constraints, and objective functions, the trajectory planning problem can be formulated in the NMPC form as follows:

$$\begin{aligned} &\min_{\boldsymbol{x}, \boldsymbol{u}} \ J(\boldsymbol{x}, \boldsymbol{u}) \\ &\text{s.t.} \ \ \dot{\boldsymbol{x}} = f(\boldsymbol{x}, \boldsymbol{u}), \boldsymbol{h}_l \le h(\boldsymbol{x}, \boldsymbol{u}) \le \boldsymbol{h}_u \\ &\qquad \boldsymbol{x}_l \le \boldsymbol{x} \le \boldsymbol{x}_u, \boldsymbol{u}_l \le \boldsymbol{u} \le \boldsymbol{u}_u, \boldsymbol{x}(0) = \boldsymbol{x}_{\text{init}} \end{aligned} \tag{20}$$

where $h(\cdot)$ is inequality constraints, include (9), (10) and (12). The allowable intervals where $h(\boldsymbol{x}, \boldsymbol{u})$, $\boldsymbol{x}$ and $\boldsymbol{u}$ are denoted by $[\boldsymbol{h}_l, \boldsymbol{h}_u]$, $[\boldsymbol{x}_l, \boldsymbol{x}_u]$ and $[\boldsymbol{u}_l, \boldsymbol{u}_u]$, these bounds include road boundary constraints, physical hard constraints and slack factor constraints. The initial trajectory $\boldsymbol{x}_{\text{init}}$ is constructed from the output of the decision-making module. Moreover, when the solution fails to converge, the initial trajectory will also be the output of this optimization problem to ensure the existence of a solution. This module employs a method that considers simplified longitudinal and lateral dynamics [34], thereby providing a high-quality initial guess for the NMPC solver and reducing the probability of convergence to infeasible or poor local minima.

The NMPC problem is solved using the FORCESPRO solver [35], with $\Delta t = 0.1$ and $N_{\text{p}} = 50$, corresponding to a 5-second optimal trajectory sequence $\boldsymbol{x}^* = \left[\boldsymbol{x}_1^*, \boldsymbol{x}_2^*, ..., \boldsymbol{x}_{N_{\text{p}}}^*\right]$.

V. Experiments and Analysis

This section discusses the validation results of MCTP on the HiL platform and the real-vehicle experimental platform.

A. Trajectory Tracking Controller Design

This study introduces a simple yet general trajectory tracking controller for closed-loop validation. The lateral control module computes the front wheel steering angle and additional yaw moment based on lateral and heading errors, while the longitudinal control module determines the longitudinal forces for each wheel by accounting for both the additional yaw moment and longitudinal error. For simplicity, the control laws are provided directly. The longitudinal error e_x, lateral error e_y and heading error e_φ for trajectory tracking are defined as:

$$\left\{ \begin{array}{l} e_x = (Y_{\text{ego}} - Y_{\text{p}}) \sin \varphi_{\text{ego}} + (X_{\text{ego}} - X_{\text{p}}) \cos \varphi_{\text{ego}} \\ e_y = (Y_{\text{ego}} - Y_{\text{p}}) \cos \varphi_{\text{ego}} - (X_{\text{ego}} - X_{\text{p}}) \sin \varphi_{\text{ego}} \\ e_\varphi = \varphi_{\text{ego}} - \varphi_{\text{p}} \end{array} \right. \tag{21}$$

where X_{ego}, $Y_{\text{ego}}$and φ_{ego} are the ego vehicle's real lateral position, longitudinal position, and yaw angle in the GCS, and X_{p}, Y_{p}, and φ_{p} are the current desired trajectory point's lateral position, longitudinal position, and yaw angle in the GCS.

The lateral control law consists of a feedforward term and a feedback term [36], [37], which can be expressed as:

$$\left\{ \begin{array}{l} \delta_{\text{f,c}} = \delta_{\text{f,c}}^{\text{FF}} + \delta_{\text{f,c}}^{\text{FB}} \\ M_{z,\text{c}} = M_{z,\text{c}}^{\text{FF}} + M_{z,\text{c}}^{\text{FB}} \end{array} \right. \tag{22}$$

where $\delta_{\text{f,c}}$ and $M_{z,\text{c}}$ represent the front wheel steering angle and the additional yaw moment. The superscripts FF and FB denote the feedforward and feedback term, respectively.

For longitudinal control, a dual-loop proportion-integral-derivative controller is used to output the required longitudinal acceleration $a_{x,\text{c}}$. Then, the longitudinal forces of each wheel $F_{\text{ij,c}}^x$ is obtained by solving a quadratic programming problem:

$$\begin{aligned} &\min_{z} \ \tfrac{1}{2} \boldsymbol{z}^{\text{T}} \mathbf{H} z + \boldsymbol{g}^{\text{T}} \boldsymbol{z} \\ &\text{s.t.} \ \ \boldsymbol{A}_{\text{eq}} \boldsymbol{z} = \boldsymbol{b}_{\text{eq}}, \boldsymbol{z}_l \le \boldsymbol{z} \le \boldsymbol{z}_u \end{aligned} \tag{23}$$

with $\boldsymbol{z} = \begin{bmatrix} F_{\text{fl,c}}^x & F_{\text{fr,c}}^x & F_{\text{rl,c}}^x & F_{\text{rr,c}}^x \end{bmatrix}^{\text{T}}$, where $\mathbf{H}$ is a 4th-order identity matrix, $\boldsymbol{g} = -2\mathbf{H}^{\text{T}} \boldsymbol{z}_{\text{p}}$, and $\boldsymbol{z}_{\text{p}}$ can computed based on the TFRM. $\boldsymbol{A}_{\text{eq}} = \begin{bmatrix} -\frac{W}{2}\cos\delta_{\text{f,c}} + l_{\text{f}}\sin\delta_{\text{f,c}} & \frac{W}{2}\cos\delta_{\text{f,c}} + l_{\text{f}}\sin\delta_{\text{f,c}} & -\frac{W}{2} & \frac{W}{2} \\ \cos\delta_{\text{f,c}} & \cos\delta_{\text{f,c}} & 1 & 1 \end{bmatrix}$, $\boldsymbol{b}_{\text{eq}} = \begin{bmatrix} M_{z,\text{c}} \\ a_{x,\text{c}} \end{bmatrix}$, $\boldsymbol{z}_l$ and $\boldsymbol{z}_u$ represent the minimum and maximum allowable longitudinal forces for each wheel.

B. HiL Experiment and Analysis

MCTP is tested on the HiL platform under two typical high-dynamics maneuver (consecutive mandatory lane-change maneuvers on high-speed and low-adhesion road conditions, as illustrated in Fig. 5 and 13) for closed-loop validation of its effectiveness and real-time performance.

1) HiL Platform and Closed-Loop Evaluation Metrics: Fig. 4 depicts the composition of the HIL platform. The host PC provides the traffic scenario and perception data. It also runs the CarSim software in real-time, providing a high-fidelity vehicle model to feedback required motion states information. The Speedgoat serves as the computational platform for algorithms. Data exchange between the host PC and Speedgoat via UDP.

Authorized licensed use limited to: BEIJING INSTITUTE OF TECHNOLOGY. Downloaded on January 18,2026 at 10:57:50 UTC from IEEE Xplore. Restrictions apply.
© 2026 IEEE. All rights reserved, including rights for text and data mining and training of artificial intelligence and similar technologies. Personal use is permitted, but republication/redistribution requires IEEE permission. See https://www.ieee.org/publications/rights/index.html for more information.

This article has been accepted for publication in IEEE Transactions on Automation Science and Engineering. This is the author's version which has not been fully edited and content may change prior to final publication. Citation information: DOI 10.1109/TASE.2026.3654151



Fig. 4. The hardware-in-the-loop platform.

To ensure a fair and quantitative evaluation, trajectory tracking errors (21) are selected as evaluation metrics for safety and feasibility. The lateral instability risk is defined as an evaluation metric for lateral instability risk, expressed as:

$$R_{\text{unstable}} = (\beta_{\text{ego}} - \beta_{\text{stable}})^2 + (r_{\text{ego}} - r_{\text{stable}})^2 \qquad (24)$$

where β_{ego} and r_{ego} represent the slip angle and yaw rate of ego vehicle, while β_{stable} and r_{stable} are their corresponding steady-state values [38].

2) HiL Experimental Case 1 Results Analysis: In this case, the ego vehicle must perform a rapid lane change on a low-adhesion road to avoid a stationary obstacle ahead while preventing a collision with a dynamic vehicle in the adjacent left lane. A detailed configuration of the scenario is illustrated in Fig. 5. The baseline method used for this case is a popular optimization-based joint trajectory planning method [10]. Furthermore, due to the challenge of generating a trackable trajectory under such extreme conditions, constraints on longitudinal/lateral acceleration and curvature are incorporated to ensure a fair comparison [14].

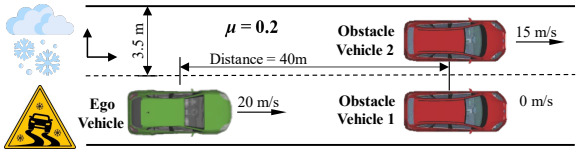


Fig. 5. The testing scenario 1 of the HiL platform experiment.

a) Open-loop Results Analysis: As shown in Fig. 6(a), the open-loop trajectories generated by the baseline method and MCTP are compared. The baseline method exhibits more abrupt lane changes, whereas MCTP enables a smoother transition between lanes. The curvature of the planned trajectory is shown in Fig. 6(b) and Table I. Both methods satisfy the continuity requirement for trajectory curvature. However, the baseline method produces higher curvature values, leading to lower feasibility, while MCTP enhances trajectory feasibility.

The maximum (Max) and root mean square (RMS) values of the lateral motion states for open-loop trajectories are presented in Table I. The baseline method, which does not account for multi-coupled dynamics, results in larger lateral motion states. In contrast, MCTP reduces these values, significantly lowering the risk of lateral instability. Using the TFRM, the

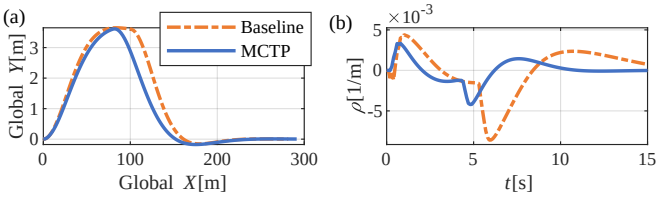


Fig. 6. Case 1 open-loop results. (a) Trajectory. (b) Curvature

TABLE I
HIL EXPERIMENT CASE 1 OPEN-LOOP RESULTS

Data	Baseline		MCTP	
	Max	RMS	Max	RMS
ρ [1/m]	-0.0086	0.003	-0.0042	0.0014
v_y [m/s]	3.4421	1.8886	-1.0255	0.3615
r [rad/s]	-0.1636	0.0573	-0.0829	0.0272
β [deg]	10.7041	5.8077	-2.9829	1.0489
require μ [/]	0.2439	0.0827	0.2	0.0711

required friction coefficient for the front left wheel under the open-loop trajectory is calculated. As shown in Fig. 7(a) and Table I, the baseline method generates a trajectory where the required road adhesion coefficient exceeds the actual available adhesion. In contrast, MCTP by considering vehicle-tire-road coupling, reduces the required adhesion coefficient, enhancing trajectory feasibility. Fig. 7(b) presents the real-time performance results. While MCTP includes more constraints, leading to slightly higher computation times than the baseline method, it still satisfies the 10Hz trajectory planning requirement.

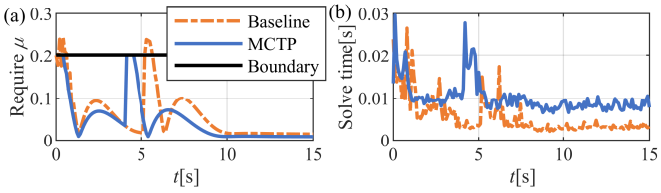


Fig. 7. Case 1 open-loop results. (a) Require μ. (b) solve time.

b) Closed-loop Results Analysis: This paragraph analyzes the closed-loop performance of trajectory planning. Fig. 8(a) illustrates the spatiotemporal relationship between the closed-loop trajectory and obstacle vehicle (OV) for both methods. In the initial phase, the baseline method rapidly adjusts the lateral position to the adjacent lane to avoid a collision with OV1. To maintain a safe distance from OV2 in the adjacent lane, it applies longitudinal braking acceleration, reducing the ego vehicle's speed (Fig. 9(a)). This maneuver demands significant lateral and longitudinal tire forces, which, under low-adhesion conditions, increase the risk of poor trajectory tracking and lateral instability. In contrast, MCTP adjusts the lateral position more smoothly, reducing the collision risk with OV1 while primarily allocating available road adhesion forces for steering to avoid a rear-end collision with OV2. Furthermore, Fig. 8(b) shows that the baseline method's closed-loop trajectory exhibits oscillations, caused by rear axle side-slip during tracking, leading to vehicle instability. Fig. 8(c) further supports this, showing higher peak yaw angles and longer oscillation durations in the baseline

Authorized licensed use limited to: BEIJING INSTITUTE OF TECHNOLOGY. Downloaded on January 18,2026 at 10:57:50 UTC from IEEE Xplore. Restrictions apply.
© 2026 IEEE. All rights reserved, including rights for text and data mining and training of artificial intelligence and similar technologies. Personal use is permitted, but republication/redistribution requires IEEE permission. See https://www.ieee.org/publications/rights/index.html for more information.

This article has been accepted for publication in IEEE Transactions on Automation Science and Engineering. This is the author's version which has not been fully edited and content may change prior to final publication. Citation information: DOI 10.1109/TASE.2026.3654151

method. In contrast, MCTP maintains a smoother trajectory with a quickly converging yaw angle, enhancing stability.

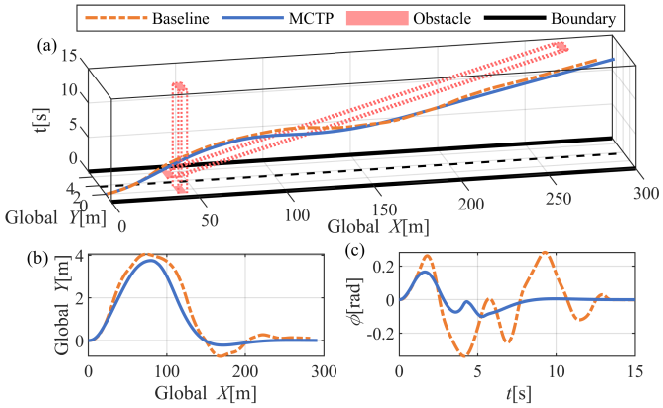


Fig. 8. Case 1 closed-loop results. (a) Spatiotemporal trajectory, (b) Trajectory, (c) Yaw angle.

TABLE II
HIL EXPERIMENT CASE 1 CLOSED-LOOP RESULTS

Data	Baseline		MCTP	
	Max	RMS	Max	RMS
v_y [m/s]	6.1978	2.7636	1.9344	0.6670
r [rad/s]	0.8107	0.4585	-0.2002	0.0719
β [deg]	18.7807	8.4263	5.5698	1.9168
ρ [1/m]	-0.0262	0.0113	-0.0100	0.0036
e_x [m]	0.8107	0.4585	0.2418	0.1788
e_y [m]	-0.5286	0.2409	0.1999	0.0805
e_φ [rad]	0.4664	0.2245	-0.1122	0.0431
R_{unstable} [/]	0.0831	0.0263	0.0072	0.0011

Fig. 9 shows the motion states of the ego vehicle during the closed-loop validation. Fig. 9(a) illustrates the longitudinal velocity variation, compared to the baseline method, MCTP reduces braking intervention when the ego vehicle needs to steer, resulting in less longitudinal velocity attenuation. This provides more reasonable control during the mandatory lane-change scenario. Fig. 9(b) displays the variations in slip angle and lateral velocity. The corresponding statistical data are shown in Table II. The max values and RMS values of the lateral motion states of the ego vehicle are smaller for MCTP. Compared to the baseline method, MCTP slightly exceeds the stability threshold but quickly converges, enhancing the lateral stability of the vehicle during extreme conditions. On the other hand, the baseline method frequently crosses the stability constraint threshold, indicating the occurrence of vehicle instability.

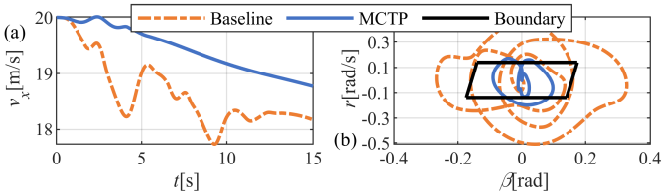


Fig. 9. Case 1 closed-loop vehicle motion states.(a) Longitudinal velocity, (b) $\beta - r$ phase plane.

The curvature variations of the ego vehicle's trajectory is illustrates in Fig. 10(a), while Table II presents the corresponding peak and RMS curvature values. The RMS curvature values are 0.0113 for the baseline method and 0.0036 for MCTP. It is evident that MCTP reduces trajectory curvature, resulting in a smoother trajectory better suited for motion control in extreme conditions. Fig. 10(b)-(d) show the accelerations in all directions during closed-loop validation. The results indicate that MCTP ensures smoother acceleration changes, minimizing frequent transitions between acceleration and braking, thereby enhancing driving comfort.

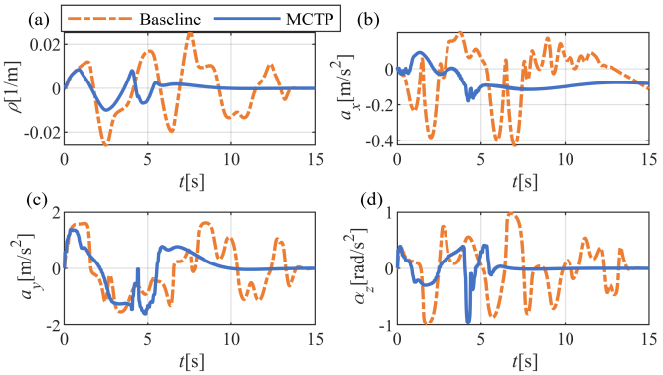


Fig. 10. Case 1 closed-loop vehicle motion states. (a) Curvature, (b) Longitudinal acceleration, (c) Lateral acceleration, (d) Yaw acceleration.

The evaluation metrics of the two methods during closed-loop validation is illustrated in Fig. 11. Whether considering longitudinal error, lateral error, or yaw angle error, tracking the MCTP-planned trajectory results in smaller tracking errors and faster convergence. Table II further confirms that MCTP improves both safety and feasibility compared to the baseline method, as reflected in its lower max and RMS tracking error values. Additionally, Fig. 11(d) and Table II highlight the risk of lateral instability, showing that MCTP reduces instability risks and provides a larger lateral stability margin.

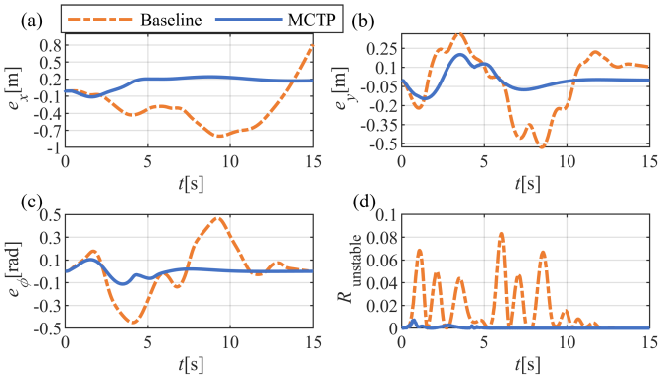


Fig. 11. Case 1 closed-loop evaluation metrics. (a) Longitudinal error, (b) Lateral error, (c) Yaw angle error, (d) Risk of lateral instability.

Fig. 12 illustrates the lateral tire force of the front left wheel, comparing the TFRM-computed results based on vehicle motion states with real values obtained from Carsim. The TFRM effectively captures tire force variations throughout

Authorized licensed use limited to: BEIJING INSTITUTE OF TECHNOLOGY. Downloaded on January 18,2026 at 10:57:50 UTC from IEEE Xplore. Restrictions apply.
© 2026 IEEE. All rights reserved, including rights for text and data mining and training of artificial intelligence and similar technologies. Personal use is permitted, but republication/redistribution requires IEEE permission. See https://www.ieee.org/publications/rights/index.html for more information.

This article has been accepted for publication in IEEE Transactions on Automation Science and Engineering. This is the author's version which has not been fully edited and content may change prior to final publication. Citation information: DOI 10.1109/TASE.2026.3654151

the vehicle's motion without requiring specific tire model parameters, validating its theoretical effectiveness.

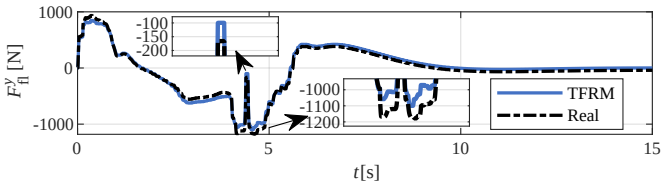


Fig. 12. Case 1 closed-loop front left wheel lateral tire force.

3) HiL Experimental Case 2 Results Analysis: In Case 2, as depicted in Fig. 13, the scenario involves more complex traffic flow. The ego vehicle must execute consecutive lane changes at high speed on a low-adhesion road to avoid collisions with four other obstacle vehicles, creating a high risk of instability and collision. Under these conditions, an ablated method that directly removes multi-coupled dynamic constraints fails to achieve effective trajectory planning and control. Therefore, to ensure a valid and fair comparison, the baseline method adopted in this case is a modified version of MCTP. Specifically, multi-coupled dynamic constraints are removed, while a vehicle dynamics envelope—coupled longitudinal and lateral acceleration constraints is introduced [27].

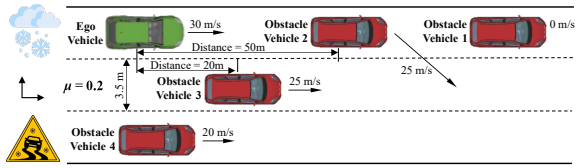


Fig. 13. The testing scenario 2 of the HiL platform experiment.

a) Open-loop Results Analysis: Fig. 14 illustrates the open-loop trajectories of the baseline method and MCTP. In terms of trajectory quality, both satisfy the condition of curvature continuity; the key difference lies in the trajectory behavior. As indicated by the statistical results in Table III, the trajectory generated by the baseline method adheres to the coupled constraints of longitudinal and lateral acceleration. Consequently, it prioritizes maintaining a greater distance from obstacles, resulting in an earlier lane change behavior.

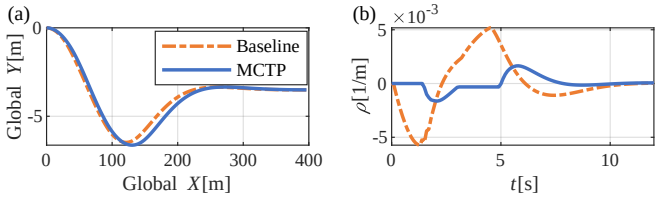


Fig. 14. Case 2 open-loop results. (a) Trajectory. (b) Curvature

In contrast, MCTP incorporates lower-level tire state considerations during planning. As shown in Fig. 15(a) and Table III regarding the required friction coefficient for the left front tire, MCTP imposes real-time strict constraints on vehicle states to ensure the required friction coefficient at each tire remains within the available road friction—even if this results in closer proximity to obstacle vehicles. The vehicle dynamics envelope used in the baseline method is constructed offline and cannot adapt dynamically to real-time vehicle states, which occasionally leads to situations where the required friction coefficient exceeds the available road friction.

TABLE III
HIL EXPERIMENT CASE 2 OPEN-LOOP RESULTS

Data	Baseline		MCTP	
	Max	RMS	Max	RMS
ρ [1/m]	-0.0057	0.0023	0.0016	0.00065
v_y [m/s]	4.3939	1.9078	3.1939	1.3183
r [rad/s]	-0.1718	0.0695	-0.0488	0.0192
β [deg]	8.4577	3.6792	6.1838	2.5443
a_x [m/s^2]	-1.8471	0.4925	-1.4700	0.4191
a_y [m/s^2]	-1.7640	0.8800	-1.4700	0.8294
α_z [rad/s^2]	0.4086	0.0987	-0.2119	0.0346
require μ [/]	0.2264	0.1069	0.2	0.0964

Regarding optimization solving time, as shown in Fig. 15(b), the increased computation in Case 2 compared to Case 1 is primarily due to the greater number of collision avoidance constraints with obstacle vehicles. The baseline method uses a pre-defined vehicle dynamics envelope with relatively fixed constraint boundaries, resulting in shorter computation times. In contrast, the multi-coupled dynamic constraints in MCTP form a dynamic nonlinear constraint with time-varying boundaries, leading to higher problem complexity. Nevertheless, even under complex traffic conditions, the solving time still meets standard planning frequency requirements (10Hz).

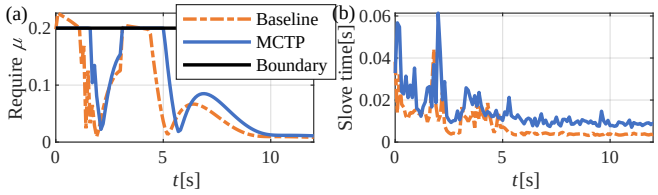


Fig. 15. Case 2 open-loop results. (a) Require μ. (b) solve time.

b) Closed-loop Results Analysis: This paragraph analyzes the closed-loop performance of trajectory planning. Fig. 16 compares the closed-loop trajectories of the baseline method and the proposed MCTP. It can be observed that MCTP achieves stabilization more rapidly after performing a series of quick lane changes, whereas the baseline method exhibits noticeable short-term oscillations before convergence. According to the quantitative metrics summarized in Table IV, the trajectory generated by MCTP leads to improved dynamic responses during tracking, exemplified by lower lateral velocity and yaw rate.

Furthermore, Fig. 17(a) depicts the longitudinal velocity profiles during closed-loop tracking. As previously mentioned, the baseline method prioritizes adherence to coupled longitudinal–lateral acceleration constraints while emphasizing obstacle avoidance, resulting in an earlier initiation of lane change and more significant deceleration. In contrast, MCTP efficiently allocates available tire–road friction to plan a feasible trajectory that satisfies both collision avoidance and tire force constraints. It allocates most of the available tire–road friction to a more

Authorized licensed use limited to: BEIJING INSTITUTE OF TECHNOLOGY. Downloaded on January 18,2026 at 10:57:50 UTC from IEEE Xplore. Restrictions apply.
© 2026 IEEE. All rights reserved, including rights for text and data mining and training of artificial intelligence and similar technologies. Personal use is permitted, but republication/redistribution requires IEEE permission. See https://www.ieee.org/publications/rights/index.html for more information.

This article has been accepted for publication in IEEE Transactions on Automation Science and Engineering. This is the author's version which has not been fully edited and content may change prior to final publication. Citation information: DOI 10.1109/TASE.2026.3654151

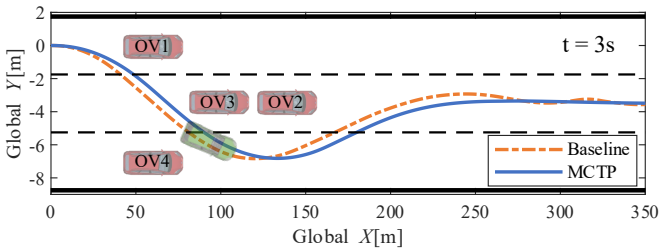


Fig. 16. Case 2 closed-loop results. (a) Spatiotemporal trajectory, (b) Trajectory, (c) Yaw angle.

gradual lane change rather than deceleration in the early phase, which is considered more rational since trajectory feasibility is fundamental to successful collision avoidance.

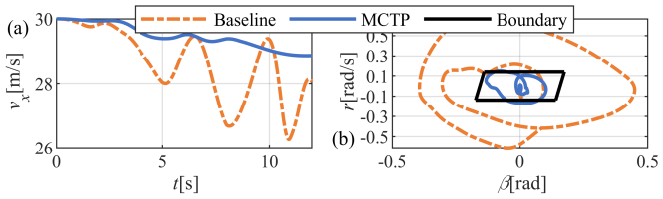


Fig. 17. Case 2 closed-loop vehicle motion states. (a) Longitudinal velocity, (b) $\beta - r$ phase plane.

The stability phase portraits depicted in Fig. 17(b) provide further insight into the closed-loop behavior. Although both methods eventually converge, MCTP demonstrates superior performance with fewer and less severe excursions beyond the stability boundaries, indicating a larger stability margin. Additionally, the RMS values of longitudinal and lateral accelerations under MCTP—listed in Table IV-are consistently lower, suggesting enhanced tracking performance under extreme driving conditions.

TABLE IV
HIL EXPERIMENT CASE 2 CLOSED-LOOP RESULTS

Data	Baseline		MCTP	
	Max	RMS	Max	RMS
v_y [m/s]	-9.9046	6.8946	-3.9312	1.8004
r [rad/s]	0.6644	0.2821	-0.1727	0.0797
β [deg]	-19.530	8.7128	-7.6034	3.4863
ρ [1/m]	0.0231	0.0099	-0.0059	0.0027
a_x [m/s^2]	-1.3320	0.4691	-0.1959	0.0899
a_y [m/s^2]	1.9526	1.1638	-1.9433	0.9838
α_z [rad/s^2]	1.0352	0.4441	-0.5379	0.1451
e_x [m]	-0.7831	0.4985	0.1974	0.0901
e_y [m]	-0.3575	0.1752	-0.2924	0.1210
e_φ [rad]	-0.4747	0.2647	0.2194	0.0938
R_{unstable} [/]	0.8809	0.1921	0.0311	0.0061

Fig. 18 and Table IV also present comparative results on tracking error and stability indices. These results reinforce the conclusion that MCTP produces more tractable and dynamically consistent trajectories. Although both methods achieve stable error convergence, the baseline method exhibits larger transient errors. For example, the max longitudinal tracking error is 0.1974 m for MCTP, compared to -0.7831m for the baseline. Moreover, the stability outcomes in Fig. 18(d) align with the observations from Fig. 17(b), confirming that the baseline trajectory entails a higher risk of instability, which is further corroborated by the higher value of the R_{unstable} metric listed in Table IV.

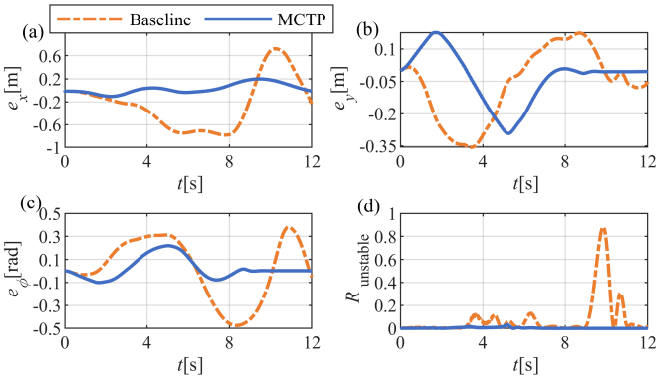


Fig. 18. Case 2 closed-loop evaluation metrics. (a) Longitudinal error, (b) Lateral error, (c) Yaw angle error, (d) Risk of lateral instability.

Fig. 19 validates the proposed TFRM. Consistent with the preceding analysis, TFRM provides generally accurate tire force predictions, despite some transient errors. Its integration into high-level planning is justified, as it enables efficient prediction of tire forces based on the planned vehicle states. This capability ensures that the resulting trajectory satisfies vehicle dynamic constraints for each tire, contributing to both safety and feasibility.

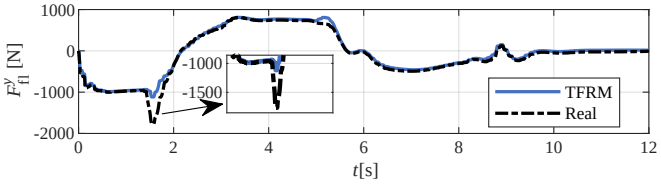


Fig. 19. Case 2 closed-loop front left wheel lateral tire force.

Furthermore, to analyze the solve time, Table V summarizes the average and maximum solve times under two experimental cases with varying numbers of obstacle vehicles (n), prediction horizons (N_p), and road adhesion coefficients (μ). The solver's computation time increases with n and N_p. Nevertheless, it consistently remains below the 100 ms planning cycle limit, thereby confirming its real-time feasibility.

TABLE V
THE SOLVE TIME UNDER DIFFERENT OBSTACLE VEHICLES n, PREDICTION HORIZONS N_P, AND ROAD ADHESION CONDITIONS μ

		Average time [ms]		Maximum time [ms]	
μ	n	$N_\text{p} = 50$	$N_\text{p} = 70$	$N_\text{p} = 50$	$N_\text{p} = 70$
0.2	2	10.1	22.2	29.5	54.2
	4	17.5	49.9	61.3	86.2
0.8	2	9.4	19.2	27.9	38.5
	4	15.6	43.6	65.7	82.2

In summary, the HiL experimental results show that MCTP effectively considers the vehicle-tire-road coupling during trajectory planning. It generates trajectories with higher safety, feasibility, and lateral stability, thus enhancing the vehicle's dynamic performance during closed-loop trajectory tracking.

Authorized licensed use limited to: BEIJING INSTITUTE OF TECHNOLOGY. Downloaded on January 18,2026 at 10:57:50 UTC from IEEE Xplore. Restrictions apply.
© 2026 IEEE. All rights reserved, including rights for text and data mining and training of artificial intelligence and similar technologies. Personal use is permitted, but republication/redistribution requires IEEE permission. See https://www.ieee.org/publications/rights/index.html for more information.

This article has been accepted for publication in IEEE Transactions on Automation Science and Engineering. This is the author's version which has not been fully edited and content may change prior to final publication. Citation information: DOI 10.1109/TASE.2026.3654151

C. Real-Vehicle Experimental and Analysis

To verify the effectiveness of MCTP, a low-adhesion continuous obstacle avoidance scenario was set up in a real-road environment. The algorithm's road adhesion coefficient was set to 0.4 to validate that MCTP effectively accounts for vehicle-tire-road coupling to plan feasible trajectory.

1) Real-Vehicle Experimental Platform: The real-vehicle experimental platform is shown in Fig. 20. The power supply box converts input power to the required levels for each device. The system employs global navigation satellite systems (GNSS) and an inertial measurement unit (IMU) for precise vehicle positioning and motion states measurement. Data is exchanged via a wireless local area network. Algorithms run on the Speedgoat real-time target machine, while CANoe receives CAN signals from Speedgoat to control the vehicle. Vehicle parameters are listed in Table VI.

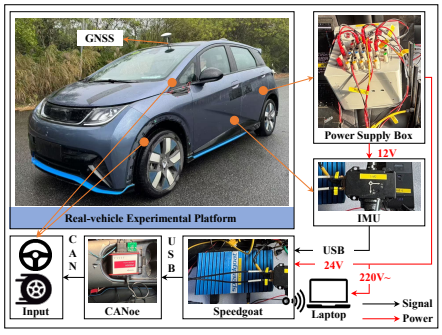


Fig. 20. The real-vehicle experimental platform

TABLE VI
PARAMETERS OF REAL-VEHICLE EXPERIMENT

Parameters	Definition	Value
m	Mass [kg]	1160
I_z	Yaw inertia [kg·m^2]	1343
l_f	Distance from CG to front axle [m]	1.0
l_r	Distance from CG to rear axle [m]	1.5
h	Height of the CG [m]	0.5
W	Wheel track [m]	1.48
L_f	Front overhang [m]	0.5
L_r	Rear overhang [m]	0.78

2) Real-Vehicle Experimental Results Analysis: Fig. 21 illustrates the trajectory curve of the real-vehicle experiment. The OV moves forward at 5 m/s, approximately 40 meters ahead of the ego vehicle, while the ego vehicle accelerates from rest and approaches. It can be observed that MCTP generates a safe trajectory that avoids collisions with the adjacent vehicle. Furthermore, the trajectory tracking controller successfully tracks the planned trajectory with high accuracy, demonstrating that MCTP ensures both the safety and feasibility of the trajectory during closed-loop experiments.

The motion states of the ego vehicle are shown in Fig. 22. Fig. 22(a) depicts the longitudinal velocity variation throughout the maneuver, including acceleration and deceleration phases, with a peak velocity of 10.6 m/s. Fig. 22(b) and (c) show the variations in lateral velocity and yaw rate. Throughout the obstacle avoidance process, the vehicle's max lateral velocity is -0.5563 m/s, and the max yaw rate is -0.0549 rad/s,

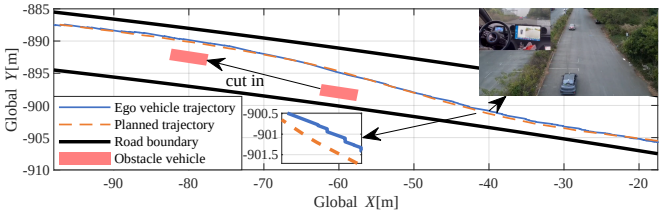


Fig. 21. Trajectory of the real-vehicle experiment.

all the vehicle's lateral motion states remain within a small range. The corresponding phase plane, shown in Fig. 22(d), further confirms that MCTP can maintain the vehicle's lateral stability constraints during closed-loop driving, generating safe, feasible, and laterally stable trajectories.

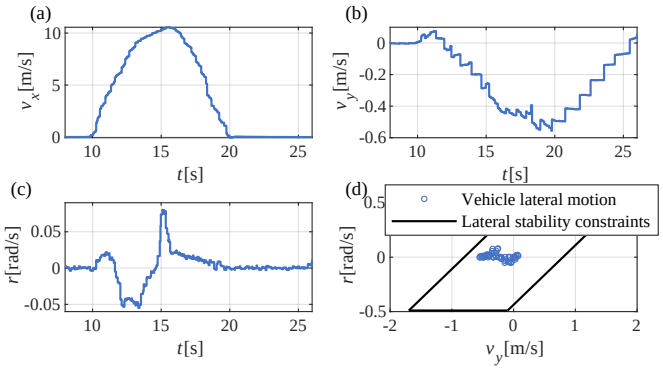


Fig. 22. Vehicle motion states of the real-vehicle experiment. (a) Longitudinal velocity, (b) Lateral velocity, (c) Yaw rate, (d) $v_y - r$ phase plane.

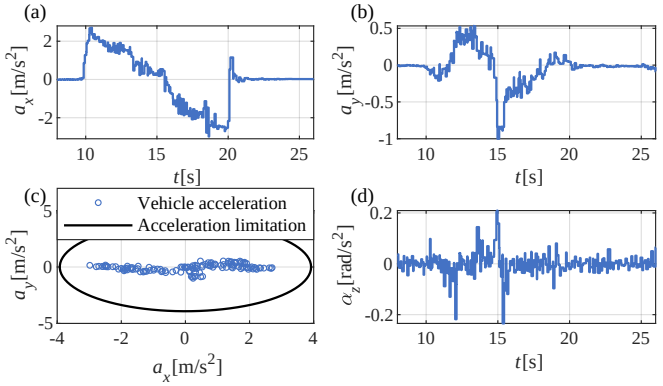


Fig. 23. Vehicle motion states of the real-vehicle experiment. (a) Longitudinal acceleration, (b) Lateral acceleration, (c) $a_x - a_y$ phase plane, (d) Yaw acceleration.

Fig. 23 displays the variations in accelerations along each direction during the continuous obstacle avoidance process. When the vehicle needs to increase its longitudinal velocity, MCTP accounts for the coupling constraints between longitudinal and lateral accelerations. It generates trajectories with minimal lateral acceleration demands while meeting the lateral collision avoidance requirements, thus improving the trajectory's feasibility. The corresponding phase plane of the lateral and longitudinal accelerations is shown in Fig. 23(c).

Authorized licensed use limited to: BEIJING INSTITUTE OF TECHNOLOGY. Downloaded on January 18,2026 at 10:57:50 UTC from IEEE Xplore. Restrictions apply.
© 2026 IEEE. All rights reserved, including rights for text and data mining and training of artificial intelligence and similar technologies. Personal use is permitted, but republication/redistribution requires IEEE permission. See https://www.ieee.org/publications/rights/index.html for more information.

This article has been accepted for publication in IEEE Transactions on Automation Science and Engineering. This is the author's version which has not been fully edited and content may change prior to final publication. Citation information: DOI 10.1109/TASE.2026.3654151

In summary, MCTP has been validated through both HiL and real-vehicle experiments. By effectively accounting for the vehicle's multi-coupled dynamics characteristics at the trajectory planning level, MCTP offers a novel approach to trajectory planning for extreme conditions.

VI. Conclusion

This paper proposes a multi-coupled dynamics trajectory planning (MCTP) scheme that considers the multi-coupled dynamics characteristics of vehicles to generate safe, dynamically feasible, and laterally stable optimal trajectories. MCTP establishes a coupled kinematics model to accurately represent vehicle motion states. Additionally, to facilitate the incorporation of tire forces into trajectory planning, a tire force representation model is developed, which eliminates the need for complex tire state. Moreover, to ensure dynamic feasibility and lateral stability, coupled dynamic constraints are formulated by leveraging tire force coupling characteristics and lateral stability analysis. Furthermore, a comprehensive set of multiple performance metrics is designed to optimize vehicle motion states, enhancing trajectory safety, feasibility, and stability. The optimal trajectory is obtained through receding horizon optimization, enabling a thorough consideration and optimization of the vehicle's multi-coupled dynamics at the trajectory planning stage. Closed-loop validation is conducted on both HiL and real-vehicle experimental platforms, demonstrating the effectiveness, real-time performance, and advantages of MCTP. In summary, MCTP advances the field of automation science by bridging vehicle theoretical control principles with real-time trajectory planning. Due to equipment limitations, high-speed real-vehicle experiments were not conducted in this study. Future work will focus on further real vehicle experiments.

Appendix
Expression of TFRM

The longitudinal and lateral tire force in the TFRM are:

$$\begin{cases} F_{\mathrm{fl}}^{x} = \frac{ma_x+F_{\mathrm{f}}}{g}\left(\frac{gl_{\mathrm{r}}}{2L} - \frac{a_x h}{2L} - \frac{a_y h l_{\mathrm{r}}}{WL}\right) \\ F_{\mathrm{fr}}^{x} = \frac{ma_x+F_{\mathrm{f}}}{g}\left(\frac{gl_{\mathrm{r}}}{2L} - \frac{a_x h}{2L} + \frac{a_y h l_{\mathrm{r}}}{WL}\right) \\ F_{\mathrm{rl}}^{x} = \frac{ma_x+F_{\mathrm{f}}}{g}\left(\frac{gl_{\mathrm{f}}}{2L} + \frac{a_x h}{2L} - \frac{a_y h l_{\mathrm{f}}}{WL}\right) \\ F_{\mathrm{rr}}^{x} = \frac{ma_x+F_{\mathrm{f}}}{g}\left(\frac{gl_{\mathrm{f}}}{2L} + \frac{a_x h}{2L} + \frac{a_y h l_{\mathrm{f}}}{WL}\right) \end{cases} \tag{A1}$$

$$\begin{cases} F_{\mathrm{fl}}^{y} = \left(\frac{ma_y l_{\mathrm{r}}+I_z\alpha_z}{L} - \frac{(ma_x+F_{\mathrm{f}})a_y h}{gL}\right)\left(\frac{1}{2} - \frac{a_y h l_{\mathrm{r}}}{gWl_{\mathrm{r}}-a_x Wh}\right) \\ F_{\mathrm{fr}}^{y} = \left(\frac{ma_y l_{\mathrm{r}}+I_z\alpha_z}{L} - \frac{(ma_x+F_{\mathrm{f}})a_y h}{gL}\right)\left(\frac{1}{2} + \frac{a_y h l_{\mathrm{r}}}{gWl_{\mathrm{r}}-a_x Wh}\right) \\ F_{\mathrm{rl}}^{y} = \left(\frac{ma_y l_{\mathrm{f}}-I_z\alpha_z}{L} + \frac{(ma_x+F_{\mathrm{f}})a_y h}{gL}\right)\left(\frac{1}{2} - \frac{a_y h l_{\mathrm{f}}}{gWl_{\mathrm{f}}+a_x Wh}\right) \\ F_{\mathrm{rr}}^{y} = \left(\frac{ma_y l_{\mathrm{f}}-I_z\alpha_z}{L} + \frac{(ma_x+F_{\mathrm{f}})a_y h}{gL}\right)\left(\frac{1}{2} + \frac{a_y h l_{\mathrm{f}}}{gWl_{\mathrm{f}}+a_x Wh}\right) \end{cases} \tag{A2}$$

References

[1] R. Chai, D. Liu, T. Liu, A. Tsourdos, Y. Xia, and S. Chai, "Deep learning-based trajectory planning and control for autonomous ground vehicle parking maneuver," *IEEE Transactions on Automation Science and Engineering*, vol. 20, no. 3, pp. 1633–1647, 2022.

[2] H. Wang, B. Lu, J. Li, T. Liu, Y. Xing, C. Lv, D. Cao, J. Li, J. Zhang, and E. Hashemi, "Risk assessment and mitigation in local path planning for autonomous vehicles with lstm based predictive model," *IEEE Transactions on Automation Science and Engineering*, vol. 19, no. 4, pp. 2738–2749, 2021.

[3] R. Chai, Y. Guo, Z. Zuo, K. Chen, H.-S. Shin, and A. Tsourdos, "Cooperative motion planning and control for aerial-ground autonomous systems: Methods and applications," *Progress in Aerospace Sciences*, vol. 146, p. 101005, 2024.

[4] X. Zhao, G. Chen, Z. Gao, J. Yao, Z. Gao, and M. Hua, "Autonomous obstacle avoidance for distributed drive electric vehicles via dynamic drifting," *IEEE Transactions on Transportation Electrification*, 2024.

[5] S. Teng, X. Hu, P. Deng, B. Li, Y. Li, Y. Ai, D. Yang, L. Li, Z. Xuanyuan, F. Zhu *et al.*, "Motion planning for autonomous driving: The state of the art and future perspectives," *IEEE Transactions on Intelligent Vehicles*, vol. 8, no. 6, pp. 3692–3711, 2023.

[6] R. Chai, A. Tsourdos, S. Chai, Y. Xia, A. Savvaris, and C. P. Chen, "Multiphase overtaking maneuver planning for autonomous ground vehicles via a desensitized trajectory optimization approach," *IEEE Transactions on Industrial Informatics*, vol. 19, no. 1, pp. 74–87, 2022.

[7] A. Arab, K. Yu, J. Yu, and J. Yi, "Motion planning and control of autonomous aggressive vehicle maneuvers," *IEEE Transactions on Automation Science and Engineering*, vol. 21, no. 2, pp. 1488–1500, 2023.

[8] R. Chai, H. Niu, J. Carrasco, F. Arvin, H. Yin, and B. Lennox, "Design and experimental validation of deep reinforcement learning-based fast trajectory planning and control for mobile robot in unknown environment," *IEEE Transactions on Neural Networks and Learning Systems*, vol. 35, no. 4, pp. 5778–5792, 2022.

[9] B. Li, Y. Zhang, T. Zhang, T. Acarman, Y. Ouyang, L. Li, H. Dong, and D. Cao, "Embodied footprints: A safety-guaranteed collision-avoidance model for numerical optimization-based trajectory planning," *IEEE Transactions on Intelligent Transportation Systems*, vol. 25, no. 2, pp. 2046–2060, 2023.

[10] G. Li, X. Zhang, H. Guo, B. Lenzo, and N. Guo, "Real-time optimal trajectory planning for autonomous driving with collision avoidance using convex optimization," *Automotive Innovation*, vol. 6, no. 3, pp. 481–491, 2023.

[11] R. Chai, K. Chen, B. Hua, Y. Lu, Y. Xia, X.-M. Sun, G.-P. Liu, and W. Liang, "A two phases multiobjective trajectory optimization scheme for multi-ugvs in the sight of the first aid scenario," *IEEE Transactions on Cybernetics*, vol. 54, no. 9, pp. 5078–5091, 2024.

[12] Y. Mi, K. Shao, Y. Liu, X. Wang, and F. Xu, "Integration of motion planning and control for high-performance automated vehicles using tube-based nonlinear mpc," *IEEE Transactions on Intelligent Vehicles*, vol. 9, no. 2, pp. 3859–3875, 2023.

[13] Q. Cui, R. Ding, C. Wei, and B. Zhou, "A hierarchical framework of emergency collision avoidance amid surrounding vehicles in highway driving," *Control Engineering Practice*, vol. 109, p. 104751, 2021.

[14] H. Chu, D. Meng, S. Huang, M. Tian, J. Zhang, B. Gao, and H. Chen, "Autonomous high-speed overtaking of intelligent chassis using fast iterative model predictive control," *IEEE Transactions on Transportation Electrification*, vol. 10, no. 1, pp. 1244–1256, 2023.

[15] Y. Qin, E. Hashemi, and A. Khajepour, "Integrated crash avoidance and mitigation algorithm for autonomous vehicles," *IEEE Transactions on Industrial Informatics*, vol. 17, no. 11, pp. 7246–7255, 2021.

[16] Y. Zhang, M. Xu, Y. Qin, M. Dong, L. Gao, and E. Hashemi, "Mile: Multiobjective integrated model predictive adaptive cruise control for intelligent vehicle," *IEEE Transactions on Industrial Informatics*, vol. 19, no. 7, pp. 8539–8548, 2022.

[17] Y. Zhang, Y. Hu, X. Hu, Y. Qin, Z. Wang, M. Dong, and E. Hashemi, "Adaptive crash-avoidance predictive control under multi-vehicle dynamic environment for intelligent vehicles," *IEEE Transactions on Intelligent Vehicles*, 2024.

[18] Y. Zhang, X. Tang, Y. Qin, and M. Dong, "Dmic: Decision-making integrated predictive control for intelligent vehicles," *IEEE Transactions on Systems, Man, and Cybernetics: Systems*, 2025.

[19] F. Tian, F.-Y. Wang, and L. Li, "Enhancing feedback steering controllers for autonomous vehicles with deep monte carlo tree search," *IEEE Robotics and Automation Letters*, vol. 7, no. 4, pp. 10 438–10 445, 2022.

[20] Y. Guo, Z. Guo, Y. Wang, D. Yao, B. Li, and L. Li, "A survey of trajectory planning methods for autonomous driving—part i: Unstructured scenarios," *IEEE Transactions on Intelligent Vehicles*, 2023.

[21] Z. Zhang, L. Zhang, J. Deng, M. Wang, Z. Wang, and D. Cao, "An enabling trajectory planning scheme for lane change collision avoidance on highways," *IEEE Transactions on Intelligent Vehicles*, vol. 8, no. 1, pp. 147–158, 2021.

Authorized licensed use limited to: BEIJING INSTITUTE OF TECHNOLOGY. Downloaded on January 18,2026 at 10:57:50 UTC from IEEE Xplore. Restrictions apply.
© 2026 IEEE. All rights reserved, including rights for text and data mining and training of artificial intelligence and similar technologies. Personal use is permitted,
but republication/redistribution requires IEEE permission. See https://www.ieee.org/publications/rights/index.html for more information.

This article has been accepted for publication in IEEE Transactions on Automation Science and Engineering. This is the author's version which has not been fully edited and content may change prior to final publication. Citation information: DOI 10.1109/TASE.2026.3654151

[22] S. Cheng, H.-N. Peng, X.-X. Dong, Z.-J. Liu, and L. Li, "Chassis global dynamics-oriented trajectory planning for automated vehicles," *IEEE Transactions on Systems, Man, and Cybernetics: Systems*, vol. 54, no. 2, pp. 950–959, 2023.
[23] X. Chen, S. Cheng, S. Li, W. Zhao, and C. Wang, "Lateral and longitudinal integrated emergency collision avoidance system with handling stability guarantee," *IEEE Transactions on Transportation Electrification*, vol. 10, no. 3, pp. 4930–4940, 2023.
[24] X. Zhang, W. Zhang, Y. Zhao, H. Wang, F. Lin, and Y. Cai, "Personalized motion planning and tracking control for autonomous vehicles obstacle avoidance," *IEEE Transactions on Vehicular Technology*, vol. 71, no. 5, pp. 4733–4747, 2022.
[25] Z. Zhang, C. Wang, W. Zhao, M. Cao, J. Liu, and K. Xu, "Path–speed decoupling planning method based on risk cooperative game for intelligent vehicles," *IEEE Transactions on Transportation Electrification*, vol. 10, no. 2, pp. 3792–3806, 2023.
[26] M. A. Sormoli, K. Koufos, M. Dianati, and R. Woodman, "A survey on hybrid motion planning methods for automated driving systems," *arXiv preprint arXiv:2406.05575*, 2024.
[27] Z. Shan, J. Zhao, B. Zhu, C. Lv, Y. Zhao, L. Ge, and S. Zhong, "Safe and efficient trajectory planning considering longitudinal and lateral coupled limits for autonomous vehicles," *IEEE Transactions on Vehicular Technology*, 2024.
[28] R. N. Jazar, *Advanced vehicle dynamics*. Springer, 2019.
[29] J. Wang, Z. Luo, Y. Wang, B. Yang, and F. Assadian, "Coordination control of differential drive assist steering and vehicle stability control for four-wheel-independent-drive ev," *IEEE Transactions on Vehicular Technology*, vol. 67, no. 12, pp. 11 453–11 467, 2018.
[30] W. Wang, T. Ma, C. Yang, Y. Zhang, Y. Li, and T. Qie, "A path following lateral control scheme for four-wheel independent drive autonomous vehicle using sliding mode prediction control," *IEEE Transactions on Transportation Electrification*, vol. 8, no. 3, pp. 3192–3207, 2022.
[31] Z. Zhu, X. Tang, Y. Qin, Y. Huang, and E. Hashemi, "A survey of lateral stability criterion and control application for autonomous vehicles," *IEEE Transactions on Intelligent Transportation Systems*, vol. 24, no. 10, pp. 10 382–10 399, 2023.
[32] F. Wang, T. Shen, M. Zhao, Y. Ren, Y. Lu, B. Feng, and G. Yin, "Lane-change trajectory planning and control based on stability region for distributed drive electric vehicle," *IEEE Transactions on Vehicular Technology*, vol. 73, no. 1, pp. 504–521, 2023.
[33] X. Zhang, A. Liniger, and F. Borrelli, "Optimization-based collision avoidance," *IEEE Transactions on Control Systems Technology*, vol. 29, no. 3, pp. 972–983, 2020.
[34] H. Fan, F. Zhu, C. Liu, L. Zhang, L. Zhuang, D. Li, W. Zhu, J. Hu, H. Li, and Q. Kong, "Baidu apollo em motion planner," *arXiv preprint arXiv:1807.08048*, 2018.
[35] A. Zanelli, A. Domahidi, J. Jerez, and M. Morari, "Forces nlp: an efficient implementation of interior-point methods for multistage nonlinear nonconvex programs," *International Journal of Control*, vol. 93, no. 1, pp. 13–29, 2020.
[36] C. Chatzikomis, A. Sorniotti, P. Gruber, M. Zanchetta, D. Willans, and B. Balcombe, "Comparison of path tracking and torque-vectoring controllers for autonomous electric vehicles," *IEEE Transactions on Intelligent Vehicles*, vol. 3, no. 4, pp. 559–570, 2018.
[37] X. Hu, Y. Zhang, Y. Hu, Z. Wang, and Y. Qin, "Time-varying gain-scheduled path-tracking controller with delay compensation (tgdc) for autonomous vehicles," 2025.
[38] R. Rajamani, *Vehicle dynamics and control*. Springer Science & Business Media, 2011.



Xuepeng Hu received the B.S. degree in vehicle engineering from the College of Mechanical and Vehicle Engineering, Hunan University in 2023. He is currently pursuing the M.S. degree in the School of Mechanical Engineering, Beijing Institute of Technology. His research interests include planning and control for autonomous vehicle.



Yu Zhang received the Ph.D. degree in mechanical engineering from the Beijing Institute of Technology, Beijing, China, in 2023. He is currently an Assistant Researcher with the China North Vehicle Research Institute. His current research interests include decision-making and dynamic control for intelligent vehicle.



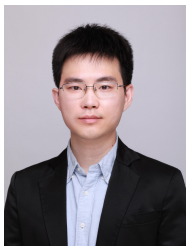
Chengye Wang received the B.S. degree in vehicle engineering from the College of Automotive Engineering, Jilin University in 2024. He is currently pursuing the M.S. degree in the School of Mechanical Engineering, Beijing Institute of Technology. His research interests include vehicle dynamics control within and beyond handling limits.



Shaoyang Shi received the B.Sc. degree in mechanical engineering from the Beijing University of Chemical Technology, Beijing, China, in 2021. He is currently working toward the Ph.D. degree in vehicle engineering with the School of Mechanical Engineering, Beijing Institute of Technology, Beijing, China. His research focuses on perception and dynamic control for intelligent vehicles.



Zhenfeng Wang received his Ph.D. degree in mechanical engineering from the Beijing Institute of Technology in 2018. From 2017 to 2018, he was a Visiting Scholar with the Department of Mechanical and Mechatronics Engineering, University of Waterloo. He is currently a Senior R&D Engineer with BYD Automotive Industry Co. Ltd and a vice Research Fellow of Beijing Institute of Technology, China. His research interests include vehicle dynamics, state estimation, and advanced chassis control.



Yechen Qin (Senior Member, IEEE) received the B.Sc. and Ph.D. degrees in mechanical engineering from the Beijing Institute of Technology, Beijing, China, in 2010 and 2016, respectively. From 2013 to 2014, he was a Visiting Ph.D. Student with Texas A&M University, USA. He was also a Postdoctoral Research Fellow and a Visiting Scholar with the Beijing Institute of Technology and University of Waterloo, Canada. He is currently an Associate Professor with the Beijing Institute of Technology. His research focuses on autonomous vehicle dynamics control. He serves as the Associate Editor for IEEE Transactions on Vehicular Technology.

Authorized licensed use limited to: BEIJING INSTITUTE OF TECHNOLOGY. Downloaded on January 18,2026 at 10:57:50 UTC from IEEE Xplore. Restrictions apply.
© 2026 IEEE. All rights reserved, including rights for text and data mining and training of artificial intelligence and similar technologies. Personal use is permitted,
but republication/redistribution requires IEEE permission. See https://www.ieee.org/publications/rights/index.html for more information.